Role of Co2C in ZnOpromoted Co Catalysts for Alcohol Synthesis from Syngas

Singh, Joseph A.; Hoffman, Adam S.; Schumann, Julia; Boubnov, Alexey; Asundi, Arun S.; Nathan, Sindhu S.; Nørskov, Jens Kehlet; Bare, Simon R.; Bent, Stacey F.

Published in:
ChemCatChem

Link to article, DOI:
10.1002/cctc.201801724

Publication date:
2019

Document Version
Peer reviewed version

Role of Co_2C in ZnO-promoted Co Catalysts for Alcohol Synthesis from Syngas

Joseph A. Singh,[a] Adam S. Hoffman,[b] Julia Schumann,[c] Alexey Boubnov,[b] Arun S. Asundi,[c] Sindhu S. Nathan,[c] Jens Nørskov,[c, d] Simon R. Bare,*[b] and Stacey F. Bent*[c]

Controlling selectivity is a key goal in the design of a heterogeneous catalyst. Herein, we present detailed characterization and activity of silica-supported cobalt catalysts modified by atomic layer deposition of ZnO. After reduction, the resulting catalysts exhibit substantial selectivity towards alcohol production during CO hydrogenation compared to catalysts containing only cobalt. The prepared catalysts have up to 46% selectivity toward alcohols with 39% of the alcohols corresponding to ethanol and other higher alcohols, albeit with reduced activity. In situ characterization of the catalyst by X-ray diffraction and X-ray absorption spectroscopy reveals details on the structural evolution in syngas, $CO + H_2$, and shows that ZnO promotion of Co results in the formation of Co_2C under catalytic conditions. A mechanism is proposed, supported by density functional theory calculations, which explains Co_2C formation by the blocking of Co step sites by Zn species. The ZnO acts a dual promoter both by facilitating Co_2C formation and by modifying the resulting Co_2C. The Co_2C formed from the ZnO-promoted Co catalysts displays improved thermal stability and selectivity compared with similar Co_2C catalysts without Zn.

Introduction

Producing chemicals and liquid fuels from renewably-generated carbon monoxide and hydrogen is an attractive route for an environmentally-sustainable economy. In the 1920's, Fischer and Tropsch discovered the possibility of synthesizing liquid hydrocarbons from syngas, a mixture of carbon monoxide and hydrogen, using heterogeneous catalysts.[1] However, there is still no industrially-suitable catalyst that is sufficiently active and selective for the formation of alcohols, from syngas, of longer chain length than methanol, which are key targets for fuel and chemical production.[2] Higher alcohols are typically produced through biofermentation, and methanol carbonylation and homologation.[2] Part of the challenge in creating selective catalysts to convert syngas to higher alcohols results from the mechanism of higher alcohol synthesis. A key step in the mechanism is CO dissociation in which the C–O bond in a chemisorbed CO molecule splits.[2–3] CO hydrogenation catalysts typically fall into a regime of low CO dissociation (resulting in methanol) or high CO dissociation (resulting in hydrocarbons).[2–3] Higher alcohols are formed through a CO insertion mechanism,[2,3b,c,4] in which CO first dissociates and is hydrogenated to form an alkyl fragment. Subsequently, a non-dissociated CO inserts into the fragment and the molecule is hydrogenated to the resulting higher alcohol. As higher alcohol synthesis requires both dissociated and non-dissociated CO, a balance in CO dissociation is required.[2,3b,c,4c] Modern work on higher alcohol synthesis has focused primarily on Rh,[5] Cu/Co,[6] Co/MoS_2,[7] and Co_2C catalysts.[4c,f]

Promoters are known to play a key role in modulating catalyst performance, in particular in higher alcohol synthesis catalysts.[2,4b,8] Previous studies have shown that the addition of Zn negatively affects the performance of Co-based catalysts for Fischer-Tropsch synthesis,[9] typically resulting in increased selectivity to lower-molecular-weight hydrocarbon products, and that ZnO addition may increase selectivity of Co catalysts towards alcohols.[10] Hence, we selected Zn to inhibit Fischer-Tropsch hydrocarbon product formation on Co and shift selectivity towards alcohols as major products. This selection was also motivated by a recent combined density functional theory and descriptor based microkinetic model study where it was concluded that "step blocking by metal oxides on transition metals such as Rh and Co will result in more selective catalysts for higher oxygenate synthesis",[5] with the hypothesis that the Zn might preferentially block the step sites.

We synthesized ZnO-modified Co catalysts using ZnO deposited by atomic layer deposition (ALD).[11] The prepared catalysts are shown to have an inverse relationship between selectivity and activity as the Zn loading is increased. High-pressure in situ studies are combined with density functional theory (DFT) to understand the nature of the catalysts through

[a] *Dr. J. A. Singh*
Department of Chemistry
Stanford University
Stanford CA-94305 (USA)
[b] *Dr. A. S. Hoffman, Dr. A. Boubnov, Dr. S. R. Bare*
SSRL, SLAC National Accelerator Laboratory
Menlo Park, CA-94025 (USA)
E-mail: simon.bare@slac.stanford.edu
[c] *J. Schumann, A. S. Asundi, S. S. Nathan, Dr. J. Nørskov, Dr. S. F. Bent*
Department of Chemical Engineering
Stanford University
Stanford CA-94305 (USA)
E-mail: sbent@stanford.edu
[d] *Dr. J. Nørskov*
Department of Physics
Technical University of Denmark
Kongens
Lyngby 2800 (Denmark)

Table 1. Parameters of as-prepared catalysts. Co and Zn loadings were determined by ICP-OES. BET surface area and BJH pore volume were determined using N_2 physisorption.

Catalyst	ZnO ALD Cycles	Co Loading [wt %]	Zn Loading [wt %]	BET Surface Area [m^2/g]	BJH Pore Volume [cm^3/g]
1 ALD-Zn/Co	1	10	1.4	240	0.90
2 ALD-Zn/Co	2	10	2.8	240	0.90
4 ALD-Zn/Co	4	10	5.6	240	0.85

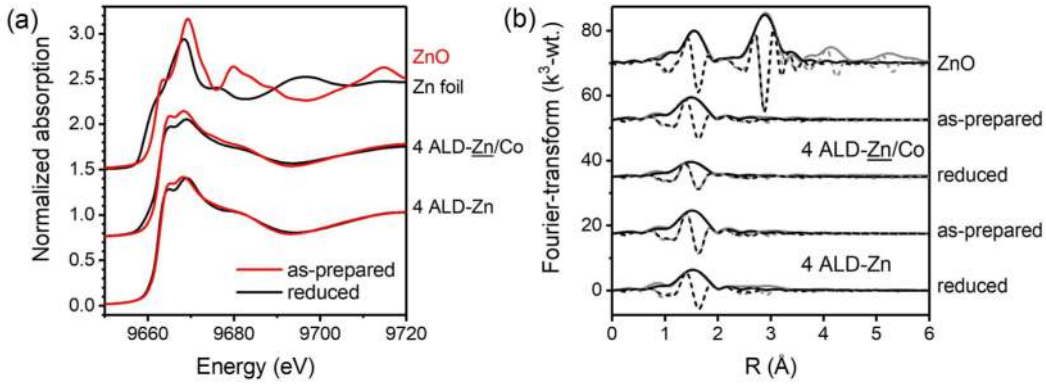

Figure 1. (a) XANES and (b) Fourier-transform EXAFS spectra measured at the Zn K-edge of a ZnO reference sample and as-prepared and reduced 4 ALD-Zn/Co and 4 ALD-Zn catalysts. In (b), the magnitude and imaginary components of the EXAFS data and best-fit models are shown. The solid lines refer to the magnitude and the dashed lines to the imaginary part of the EXAFS spectra. The experimental data are shown with grey lines and the fit with black lines. Corresponding EXAFS spectra in *k*-space are shown in Figure S4.

their catalytic lifecycle. By means of in situ X-ray diffraction (XRD) and X-ray absorption spectroscopy (XAS) we investigate the bulk and electronic structures of these catalysts, and combine these data with ex situ surface characterization. Interestingly, we find that rather than only blocking step sites, the ZnO modification results in the conversion of the cobalt nanoparticles to Co_2C nanoparticles under reaction conditions. Thus we compare the catalytic results from a synthesized silica-supported unpromoted Co_2C catalyst for comparison. Using DFT, we propose that Zn selectively binds to the high index Co surfaces and provide an explanation for why Zn results in Co_2C formation, which in turn is selective toward higher alcohols.

Results and Discussion

The physical properties of the ALD ZnO-modified catalysts are presented in Table 1. Cobalt catalysts supported on silica (Co/SiO_2, referred to herein as Co), were modified using ZnO ALD,[12] depositing 17 mg ZnO per gram of catalyst in each ALD cycle as determined by inductively coupled plasma optical emission spectrometry (ICP-OES). The ZnO-modified catalysts will be referred to as "ALD-Zn/Co" with the notation "4 ALD-Zn/Co" referring to a Co catalyst prepared with 4 cycles of ZnO ALD. There was a modest decrease in the Brunauer-Emmett-Teller (BET) surface area from 260 m^2/g for the initial unmodified Co catalyst to 240 m^2/g for 4 ALD-Zn/Co, and there was a small decrease in the Barett-Joyner-Halenda (BJH) pore volume from 0.90 mL/g for the initial unmodified Co catalyst to 0.85 mL/g for 4 ALD-Zn/Co.

The results of powder XRD of the calcined Co and 4 ALD-Zn/Co catalysts are presented in Figure S1. The only crystalline phase identified in these fresh catalysts is Co_3O_4 (PDF card 00-042-1467), each with similar average crystallite size (~13 nm) determined by Scherrer analysis (Table S1). It was not possible to identify any crystalline Zn-containing phase for the as-prepared 4 ALD-Zn/Co catalyst, indicating that the ZnO is either amorphous and/or highly dispersed. The XAS spectra of the calcined catalysts are presented in Figures S2 and S3. Both the Co K-edge X-ray absorption near-edge structure (XANES) spectra and the extended X-ray absorption fine structure (EXAFS) spectra of the two samples are in excellent agreement with those from the Co_3O_4 standard (Figures S2 and S3). This visual assignment was confirmed by detailed EXAFS modeling, and the results are presented in Figure S3b and Table S2.

The Zn K-edge XANES of the as-prepared 4 ALD-Zn/Co catalyst (Figure 1a) had an edge position similar to that of ZnO. However, the spectrum differed in post-edge structure. The best-fit EXAFS model characterizing the as-prepared 4 ALD-Zn/Co catalyst collected at the Zn K-edge corresponded to a highly dispersed oxidized Zn structure with Zn surrounded by six O atoms at a bond length similar to ZnO (Figure 1b, Figure S4 and Table S3). Importantly, it was not possible to model any next nearest neighbor scattering in the data, e.g. due to Zn–Zn scattering through a Zn–O–Zn bridge, that would be expected for an extended ZnO-like structure. The deviation in the EXAFS fitting from the ZnO structure agrees with the XANES results showing that the data did not match the ZnO standard. Similar to this result, Camacho-Bunquin *et al.* found that for thin ZnO ALD films deposited on SiO_2, Zn–O short-range scattering was

present with no second shell scattering.[12a] Prior work found that with increasing ZnO film thickness deposited by ALD, the magnitude of the second shell Zn–Zn scattering increased as expected for a ZnO structure,[12a,13] but due to the low amount of ZnO deposited in this study we did not observe this.

Thus, both the EXAFS and XRD data of the as-prepared, calcined 4 ALD-Zn/Co (and Co) catalysts are in agreement, and indicate that the cobalt is present as nanoparticles (~13 nm diameter) with a Co_3O_4 structure. The addition of the ALD ZnO results in a highly dispersed oxidic zinc with a ZnO-like structure possesing only short-range order.

In order to provide some insight regarding the surface properties of the catalysts we used CO chemisorption and XPS. The CO chemisorption data are presented in Table S4. The addition of the ZnO by ALD lowers the CO uptake capacity by an order of magnitude, suggesting that the ZnO covers the surface of the Co NPs. This conclusion is supported by the XPS data, Figure S5 and Table S5, which show that the surface atomic concentration of the Co is lower after the 4 ALD-Zn treatment. The Co $2p_{3/2}$ binding energy of the as-prepared 4 ALD-Zn/Co catalyst (Figure S6) is consistent with that expected for Co_3O_4 [14], in agreement with the XRD and XAS data. The Zn $2p_{3/2}$ binding energy (Figure S7) is consistent with the Zn being present as ZnO[15], in agreement with the XAS.

The as-prepared catalysts were activated in a flow of hydrogen at 450 °C for one hour prior to catalytic testing. The reduction of the cobalt was followed using in situ temperature programmed reduction (TPR) XANES (Figure 2a) and by XRD (Figure 2b). Linear combination fitting (LCF) of the XANES data, using appropriate reference standards (Co_3O_4, CoO and Co), was performed to quantitatively determine the amount of each cobalt species as a function of reduction temperature, and the results are plotted in Figure 2c. The reduction of the cobalt proceeds via a CoO phase to metallic cobalt.[16] The relative phase analysis of the XRD reduction profiles (Figure 2c) are in good agreement with those from the XANES data. The corresponding TPR XANES spectra and XRD data of the Co-only catalyst are shown in Figure S8.

The in situ XRD measurements of the final reduced 4 ALD-Zn/Co and Co catalysts show that Co is present in the *fcc*-Co phase (PDF card 00-015-0806) in both (Figure S9). Likewise, the EXAFS modelling of the final reduced catalysts (χ(k) XAS data and model in Figure S10, FT XAS data and model in Figure S11) are consistent with the Co being present only as metallic Co nanoparticles (Table S6). There was some residual CoO (PDF card 00-048-1719) present after in situ reduction in the XRD measurement, but not in the XAS data. This small difference can be rationalized due to the catalyst being reduced for a longer period in the in situ XANES measurement as it was heated at 5 °C/minute as opposed to 10 °C/minute for the in situ XRD measurement.

In situ Zn K-edge XAFS of the reduced 4 ALD-Zn/Co catalyst are presented in Figure 1 and results of the EXAFS modeling are summarized in Table S3. After reduction, a small shoulder was present on the rising absorption edge (Figure 1a), together with a decrease in the intensity of the white line and a decrease in the Zn–O coordination number (CN) from 3.6 to 2.9 (Table S3).

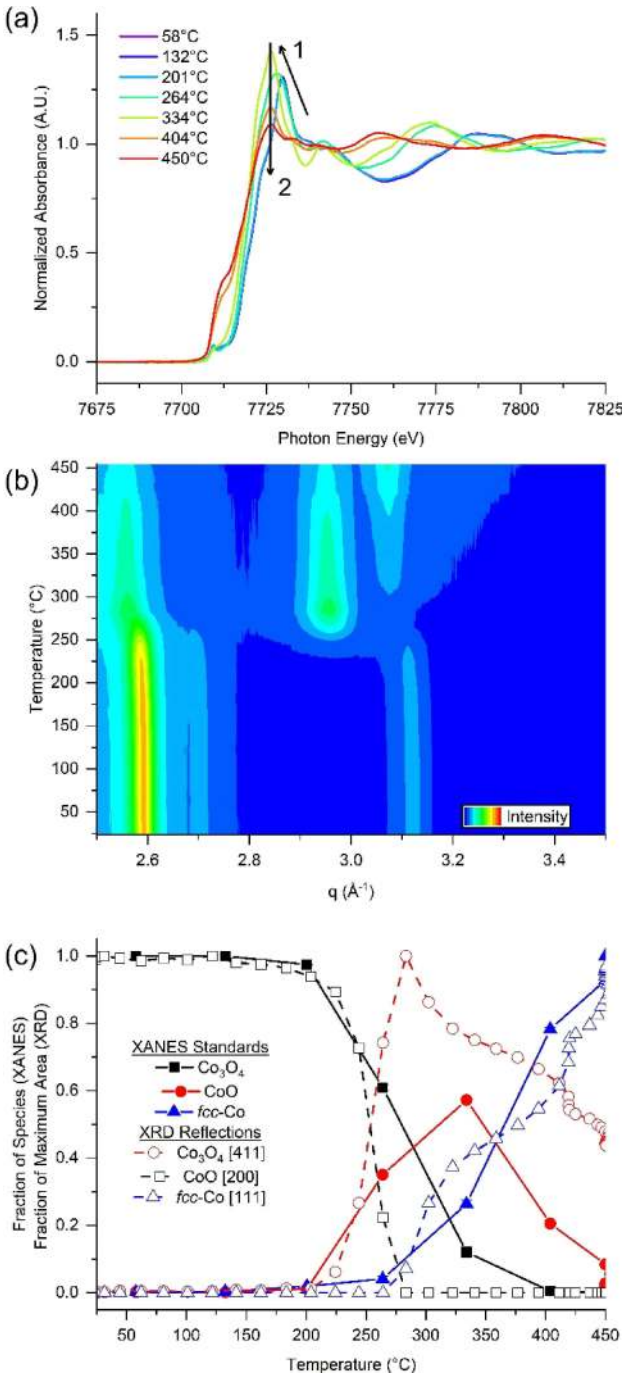

Figure 2. *In-situ* Co K-edge XANES (a), and XRD (b), during temperature programmed reduction of 4 ALD-Zn/Co catalyst in flowing H_2 as temperature was ramped from 25 °C to 450 °C at 10 °C/min. Linear combination fitting of the XANES spectra (solid) and crystallographic phase analysis of the XRD diffraction patterns (dashed) (c) of 4 ALD-Zn/Co show a two-step reduction process. XANES spectra of bulk Co_3O_4, CoO, and *fcc*-Co were used as standards during the LCF analysis with the Co_3O_4 (411), CoO (200), and *fcc*-Co (111) diffraction peaks use for XRD phase analysis.

The small shoulder occurred at a similar energy to the rising edge of Zn metal (Figure 1). These observations suggested that there was a small a fraction of the oxidic zinc that was reduced to metallic Zn. However, we have not been successful in adding

Table 2. Performance of Co catalysts at 250 °C and 20 bar syngas (2:1 H_2:CO) with varying Zn loadings;. C_{2+} OH refers to primary alcohols with chain length greater than one C. HC refers to hydrocarbons (alkanes and alkenes). Performance data shown is an average over at least 3 hours of data acquired after the catalysts reached steady-state (minimum 6 hours). The uncertainties were determined through 3 replicate experiments. All measurements were performed at approximately 1 % conversion.

Catalyst	Selectivity [C%] MeOH	C_{2+} OH	CH_4	C_2–C_4 HC	C_5–C_9 HC	Activity[a]
1 ALD-Zn/Co	14 ± 3 %	16 ± 1 %	38 ± 1 %	21 ± 4 %	10 ± 4 %	29 ± 0.3
2 ALD-Zn/Co	17 ± 4 %	18 ± 1 %	39 ± 4 %	21 ± 2 %	5 ± 3 %	24 ± 3
4 ALD-Zn/Co	28 ± 6 %	18 ± 3 %	32 ± 4 %	19 ± 1 %	2 ± 1 %	12 ± 4
Co_2C/SiO_2	10 %	9 %	52 %	21 %	8 %	92

[a] Activity is expressed in μmol CO converted per gram catalyst per minute.

a Zn–Zn scattering path from Zn metal in the modeling of the EXAFS data (Figure 1b). This suggests that the amount of Zn that was potentially reduced was on the order of a few percent. An identical treatment of a 4 ALD-Zn sample (i.e. ZnO deposited on silica without Co), exhibited neither any indication of an oxidation state change nor a decrease in the Zn–O coordination number, but instead indicated a slight degree of aggregation of the dispersed ZnO-like phase. There was a slight increase in the magnitude of the FT at a distance where a peak due to Zn–O–Zn would occur (Figure 1). These results suggest that only a portion of Zn, perhaps the Zn in contact with Co, was reduced and thus contributed to the catalytically active phase.

It was not possible to include a Zn–Co scattering path for the Zn containing sample in the modeling of the Co K-edge EXAFS data, suggesting that if there was any Zn–Co alloy/bimetallic formation then it was below the detection limit of the technique. In agreement with this, the Zn K-edge data on the reduced 4 ALD-Zn/Co sample is consistent with a small amount of the Zn being reduced, but insufficient to determine the local bonding environment.

Taken together, the in situ XRD and XANES/EXAFS results are consistent in determining that the catalysts were reduced to primarily the metallic Co phase after the activation (reduction) process. The reduced 4 ALD-Zn/Co catalyst consisted of primarily *fcc*-Co nanoparticles supported on the silica with also the possibility of residual CoO, depending on the details of the reduction process. Scherrer analysis indicated the size of the Co nanoparticles have a diameter ~10 nm (Table S1). The same conclusions can also be drawn for the unmodified Co/SiO_2 catalyst.

Following the activation, the catalysts were tested for syngas conversion at 250 °C, and 20 bar syngas (2:1 H_2:CO). We note that for the catalytic testing the flow rate and catalyst charge values were chosen to maintain CO conversion below 2 % in order to ensure differential reaction conditions and minimize secondary reactions. The catalysts took at least six hours for the conversion to reach steady state, during which time the selectivity to alcohols increased. The selectivity for alcohols and activity for the catalysts is presented in Table 2.

The data in Table 2 show that all of the ZnO-modified catalysts exhibited selectivity towards alcohols, with selectivity towards methanol increasing, the selectivity towards hydrocarbons decreasing, and long-chain C5-C9 hydrocarbons becoming trace products, as the number of ALD ZnO cycles was increased. These product selectivity data are substantially different to a typical Co-only Fischer-Tropsch catalyst (Table S7 presents the comparable data for the Co catalyst). The addition of ZnO suppresses hydrocarbon formation while the rate of methanol and higher alcohol formation is relatively unaffected.

In order to understand the structural changes in the catalyst during reaction, especially with the addition of the ZnO, we followed the catalyst structure under operating conditions (250 °C, 20 bar 2:1 H_2:CO) using XAS and XRD. The results of these measurements are presented in Figure 3 (XRD for 4 ALD Zn/Co), Figure 4 (steady-state XANES and EXAFS), Figure S12 (time-resolved XANES), Figure S13 k-space EXAFS for 4 ALD-Zn/Co, Figure S14 for k-space EXAFS for Co, and Figure S15 XRD for Co.

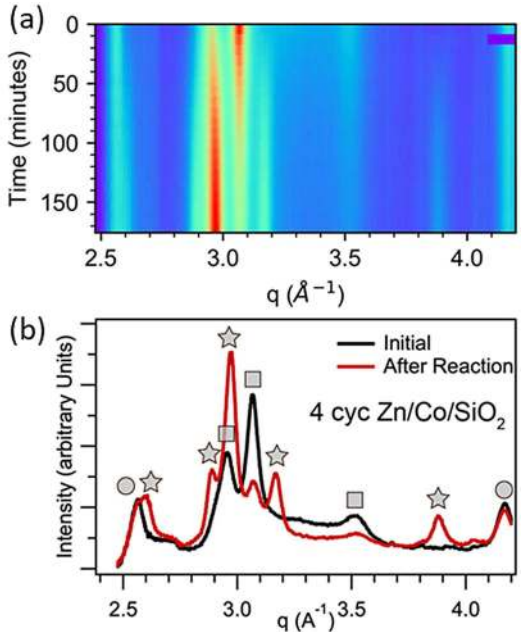

Figure 3. *In-situ* XRD (a) performed in 20 bar 2:1 H_2:CO at 250 °C of 4 ALD-Zn/Co catalyst shown as a function of time on stream. In (b), the XRD pattern for the 4 ALD-Zn/Co catalyst is shown in its initial reduced state and after treatment at reaction conditions with reflections due to CoO (●), *fcc*-Co (■), and Co_2C (★) marked.

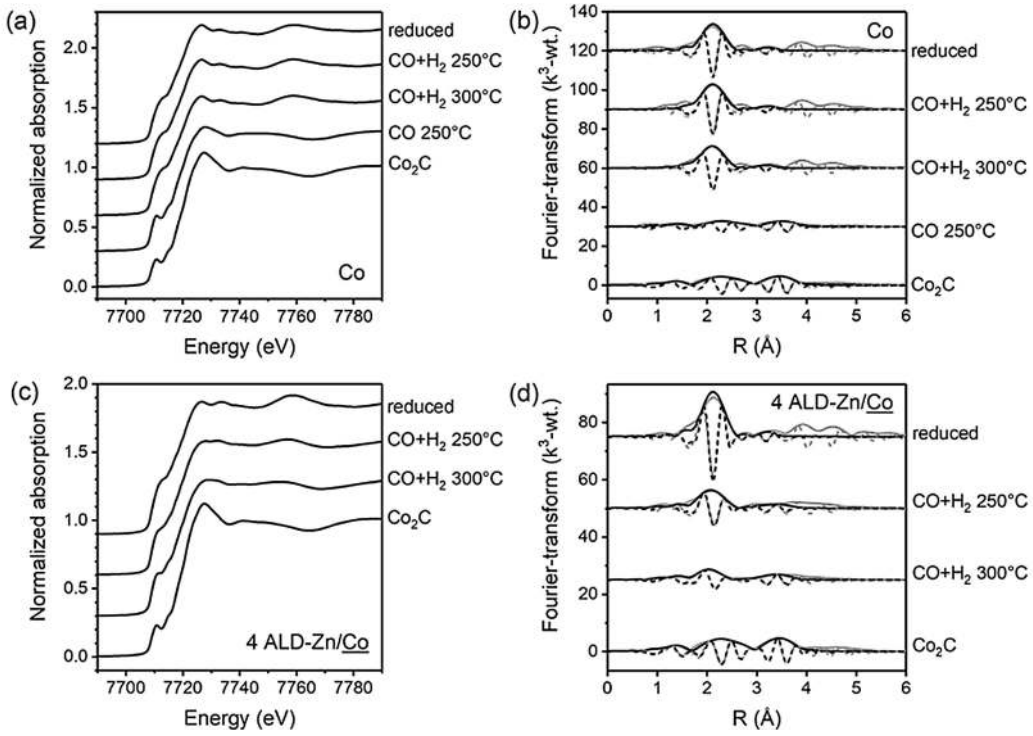

Figure 4. (a, c) Co K-edge XANES and (b, d) the Fourier-transform of the EXAFS spectra of (a, b) Co and (c, d) 4 ALD-Zn/Co catalysts after reduction, at steady state at 250 °C in 20 bar syngas and at steady state at 300 °C in 20 bar syngas. The spectra of Co after exposure to 250 °C in 20 bar CO and Co_2C are provided as references. The solid lines refer to the magnitude and the dashed lines to the imaginary part of the EXAFS spectra. The experimental data are shown with grey lines and the fit with black lines. Corresponding EXAFS spectra in *k*-space are shown in Figure S10 and Figure S11.

The XRD of the 4 ALD-Zn/Co catalyst showed the emergence of new reflections during reaction, as seen in Figure 3a. These new reflections are assigned to Co_2C (PDF card 04-004-4639), which formed at the expense of the *fcc*-Co phase, as evident from the decrease in, but not complete removal of, reflections from *fcc*-Co. The intensity of CoO reflections remained essentially unchanged during the reaction, indicating that any residual CoO did not convert to Co_2C under these conditions (Figure 3b).

Distinct changes were also observed for the 4 ALD-Zn/Co catalyst by in situ Co K-edge XANES as a function of time on stream in the syngas at 20 bar, with the emergence of a more well-defined pre-edge shoulder (Figure S12b). The distinct pre-edge shoulder at 7710.8 eV (Figure 4c) is associated with the presence of Co_2C[17] and we also observed a similar feature in our synthesized Co_2C reference (Figure 4c). The pre-edge feature on the 4 ALD-Zn/Co catalyst was not as pronounced as in the Co_2C reference, suggesting an incomplete carburization of 4 ALD-Zn/Co catalyst, in agreement with the in situ XRD.

Modeling of the Co K-edge EXAFS data for the 4 ALD-Zn/Co was conducted to provide further structural information on the cobalt species present under reaction conditions after reaction with 20 bar syngas both at 250 °C and at 300 °C. The best-fit EXAFS model characterizing the 4 ALD-Zn/Co catalyst (Figure 4d and Table S8) was consistent with the presence of a combination of Co_2C and Co metal. The arrangement of Co atoms in a Co_2C lattice is the same as in *hcp*-Co,[18] but the presence of the carbon atoms results in an increase in the lattice constant and distortion of the Co lattice. Thus, the Co_2C modelling of the EXAFS data included both Co–C and Co–Co single-scattering paths. These paths have a distribution of bond lengths, resulting in many multiple-scattering paths. The resulting superposition of paths (e.g. Co–Co single-scattering) with varying bond distance was strongly destructive due to summation of positive and negative values, resulting in a low total amplitude of the EXAFS spectrum (Figure S15 and S16). Thus, the data indicate that during syngas reaction, the cobalt in the 4 ALD-Zn/Co catalyst was present as a mixture of Co_2C and Co, as also seen in the XRD and XANES measurements.

Interestingly, the degree of carburization determined using the Co K-edge EXAFS data was found to increase with temperature (Figure 4d and Table S8), with the Co_2C fraction determined as 52 mol.% at 250 °C rising to 70 mol.% at 300 °C, based on scaling factors of the Co_2C and Co models in Table S8. Using the relative intensity ratio method, the XRD measurements indicate a Co_2C conversion of approximately 60 mol.% at 250 °C, in reasonable agreement to that determined from EXAFS.

The in situ Zn K-edge XAFS results for the 4 ALD-Zn/Co catalyst after reaction with syngas at 250 °C and 300 °C are presented in Figure S17, Figure S18 and Table S9. The parameters of the best-fit model have no significant changes from the activated (reduced) form of the catalyst. The weak pre-edge shoulder, indicative of metallic Zn presumed to be from the

reduced species in contact with Co, was still present. The dominant Zn XAFS signal originates from an oxidic Zn moiety.

A summary of the reaction selectivity and the catalyst phases during exposure to syngas at 250 °C is presented in Figure 5 for the 4 ALD-Zn/Co catalyst. Phase data detected

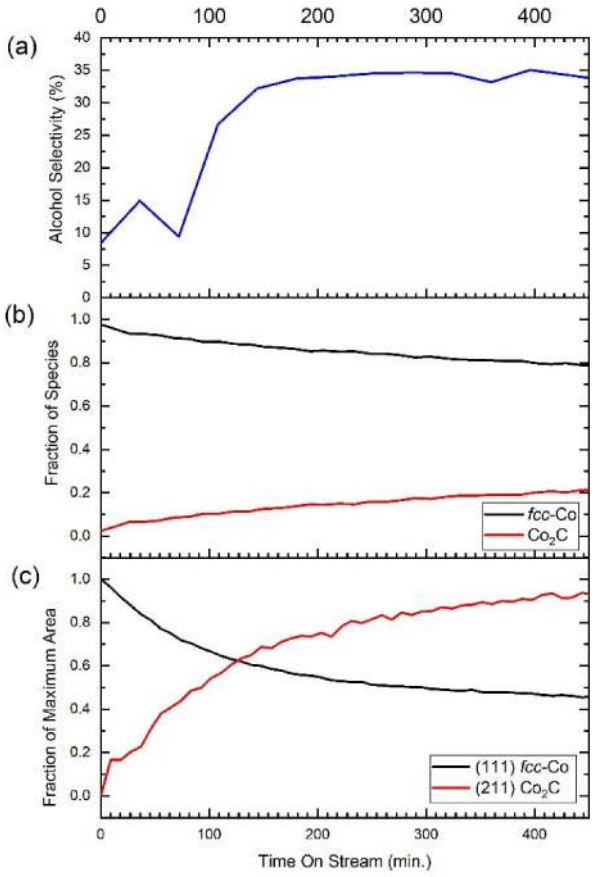

Figure 5. (a) Selectivity to alcohols and phase analysis of 4 ALD-Zn/Co using (b) Co K-edge XANES and (c) XRD in 20 bar 2:1 H_2:CO at 250°C. In (b) the quantified amount of Co and Co_2C were determined using linear combination fitting (LCF) to the XANES data in Figure S8. In (c), phase changes were determined by integrating the area of *fcc*-Co (111) and Co_2C (211) reflections (black and red, respectively).

using XRD and phases quantified using LCF-XANES are shown in Figure 5c and 5b, respectively, over the same time of catalytic testing. Over the first hour, there appears to be an induction period in the alcohol selectivity (Figure 5a) after which the selectivity increases sharply and then remains constant. The relative activity after the induction period appears to rise more slowly. If the timescales for these observations are compared to the evolution of the cobalt phases determined from the XANES (Figure 5b) and XRD (Figure 5b), then to a first order approximation the timescales for the conversion of the metallic Co to Co_2C and the activity are all similar, suggesting that the catalytically active phase is actually Co_2C and not metallic Co. The selectivity reaches steady-state faster than the catalyst's bulk carbide content (Figure 5c). If we assume a mechanism in which the Co nanoparticles carburize from the surface inwards, and because only the surface of the exposed carbide is relevant for the catalyst performance, then the catalyst's selectivity would be expected to reach a steady state faster than the catalyst's bulk carbide content. The nanoparticles then continue to carburize as a function of time on stream, and this continued carburization affects primarily the activity. We attribute the slight differences in the timescales of the XRD and XANES measurements to the fact that the XRD and XANES measurements were performed in different reactors; differences in the measured temperature in each reactor could account for these discrepancies since the formation of the Co_2C is a strong function of reaction temperature.

As discussed above, the appearance of the unexpected Co_2C phase in the ALD ZnO catalysts for which high alcohol selectivity was observed suggests that Co_2C may be responsible for the high selectivity. In order to check for correlations between the carbide formation on ZnO-promoted Co and alcohol selectivity, we prepared a control sample of Co_2C by carburizing a Co catalyst, discussed in detail below. Unlike the 4 ALD-Zn/Co catalysts, the Co_2C catalyst did not have any residual metallic Co as verified using XRD (Figure S19). We compared the performance of this catalyst to the 4 ALD-Zn/Co catalysts, and the results are shown in Table 2. The Co_2C catalyst also shows selectivity to the alcohols, albeit with lower selectivity than the ALD Zn/Co catalysts, with low selectivity to hydrocarbons, and thus does not perform as a Fischer-Tropsch catalyst.

To prepare the carburized Co catalyst, the Co-only catalyst was exposed to a flow of pure CO at 20 bar and 250 °C for 7 hours. After this reaction, the only crystalline phase detected by XRD was Co_2C, with no bulk metallic Co detected (Figure S19). The Co K-edge EXAFS of this catalyst is presented in Figure 4, Figures S14, and Table S8, and is labelled as "CO 250 °C". Interestingly, for the catalyst exposed to these reaction conditions, the Co K-edge EXAFS data fits to Co_2C but additional Co–C–O multiple-scattering paths due to linearly adsorbed CO are required for satisfactory modeling, indicating that the cobalt carbide nanoparticles are covered by adsorbed carbonyl ligands (Figure S16). The strong forward-scattering between the Co absorber and the carbon and oxygen of the carbonyl are characteristic of adsorbed CO. The set of paths per linearly adsorbed CO included Co–C and Co–O single-scattering, equivalent three-legged Co–O–C-Co and Co–C–O-Co multiple-scattering (hence double degeneracy), and four-legged Co–C–O-C–Co multiple-scattering. Single scattering Co–C and Co–Co paths present in $Co_2(CO)_8$ were not accounted for here, since they were already represented by the ones in the Co_2C model. The Co–C–O multiple-scattering was not observed on the Co and 4 ALD-Zn/Co catalysts as it was possibly obscured by the stronger Co–Co scattering signal present for these catalysts.

In stark contrast to the 4 ALD Zn/Co catalyst, the Co catalyst (which also starts as a mixture of primarily *fcc*-Co with some CoO after reduction, as described above) shows no measurable changes in the diffraction peak positions or widths under reaction conditions, showing the high stability of the Co catalyst in its metallic state under reaction conditions (Figure S15) in

agreement with prior studies.[16a,19] Similarly, the Co K-edge XANES (Figure S12a) shows no significant changes while exposed to syngas. This observation is also in line with prior studies.[19b,20] The EXAFS data and the results of the best-fit modeling from the Co catalyst are presented in Figure 4b and Table S8, respectively. The cobalt remained as metallic nanoparticles in the Co catalyst after exposure to reaction conditions at both 250 °C and 300 °C, and no significant changes in either the CN or Co–Co bond length were observed in the Co K-edge EXAFS. This result is in agreement with prior studies using in situ XAFS to study Co catalysts during syngas exposure.[19b,20]

The spent 4 ALD-Zn/Co and Co_2C catalysts were also studied using ex situ techniques. STEM-EDS mapping of the spent 4 ALD-Zn/Co catalyst (Figure S20) suggests that ALD results in ZnO covering both the surface of the silica support and the cobalt NPs. The surface properties of the spent catalysts were probed using XPS. As shown in Figure S6, the Co $2p_{3/2}$ peak is shifted to lower binding energy (777.8 eV) compared to the fresh catalyst, and is consistent with the binding energy of Co_2C,[21] and the C 1s peak (Figure S21) shows a peak consistent with carbide.[21] The Zn $2p_{3/2}$ peak is little affected by the reaction. All three of these observations are consistent with the surface of the catalyst nanoparticles being in a similar chemical state to the interior, as established from the in situ XRD and XAS measurements. It is also noteworthy that there is a significant difference in the relative intensity of the C 1s peaks between the 4 ALD Zn/Co and Co catalysts (Fig. S21 and Table S5). The data from the Co is consistent with a high amount of coke deposited on the catalyst, as expected for typical Co-catalyzed Fischer-Tropsch producing high molecular weight hydrocarbons. The spent 4 ALD Zn/Co catalyst is essentially adsorbed carbon-free.

One other interesting discovery was a difference in stability between the Co_2C phases in Co_2C and 4 ALD-Zn/Co catalysts. We compared the stability of these two catalysts by heating in H_2 while monitoring using XRD as shown in Figure S22. The Co_2C catalysts decomposed at 250 °C in H_2. This result agrees with prior work showing that temperatures below 200 °C are high enough to decompose Co_2C in H_2.[17b,22] Upon decomposition, the Co_2C catalyst formed *hcp*-Co.[17b,18] On the other hand, the Co_2C phase in the 4 ALD-Zn/Co catalyst was stable in H_2 at 250 °C and only decomposed to *hcp*-Co when heated above 360 °C. We postulate that this enhanced stability of the Zn-promoted Co_2C-phase is related to the surface structure and the destabilization of carbon on the Co surfaces in the presence of Zn, since the bulk structures of Co_2C in both post-conversion-reaction 4 ALD-Zn/Co and Co_2C were similar. The enhanced stability of Co_2C in the presence of Zn further demonstrates that the Zn is indeed modifying the surface of Co_2C.

Based on the differences in catalytic selectivity of the carbided catalysts with and without Zn, it is clear that the presence of Zn in the Co catalyst system plays an important role in the syngas conversion activity and selectivity. In the following, we provide evidence from DFT calculations and experimental results that the role of the Zn is twofold. First, we posit that the presence of Zn facilitates the formation of Co_2C under conditions in which Co would not normally form the carbide. Second, we propose that the Zn also blocks less-selective sites on the Co_2C surface to allow for higher selectivity toward alcohols.

To understand the role of Zn, we must first determine what phase of Zn is energetically stable under catalytic conditions. Under the reaction conditions used in this study (−2.6 eV O chemical potential, or 523 K, 10^{-2} bar H_2O, 13.3 bar H_2), bulk ZnO is more stable than bulk Zn based on the relative Gibbs free energies (Table S7). On the other hand, DFT calculations show that at the Co surface, metallic Zn is energetically favored over ZnO species. DFT calculations were performed for slabs of crystalline Co, and the resulting Gibbs free energies of metallic Zn and ZnO supported on Co (111) and Co (211) surfaces, each relative to bulk ZnO, are presented in Table S10. It can be seen that the structure with a surface layer of ZnO on the Co (111) surface is less stable than the corresponding bulk Co and ZnO species, indicating that there is limited interaction of ZnO on the Co (111) surface. Although ZnO is stabilized on the Co (211) surface under reaction conditions, the data show that metallic Zn is energetically favored on Co (211) compared to a ZnO surface layer on Co (211). Hence, we conclude that metallic Zn is likely present at the Co surface under these catalytic conditions. This conclusion is consistent with the subtle changes of the Zn K-edge XAFS that we noted during the reduction and catalytic reaction. The presence of metallic Zn is also supported by literature studies of related Cu/ZnO methanol synthesis catalysts, for which metallic Zn forms on the Cu surfaces despite bulk metallic Zn being unstable.[23]

The data in Figure 6 reveal that the presence of Zn on Co catalysts promotes the formation of Co_2C under syngas reaction conditions. Similar to Zn in this work, the addition of promoters such as Na[8a,24] and CaO[25] are also known to promote the formation of Co_2C. To understand the mechanism by which Zn promotes Co_2C formation, we first look to these other systems for inspiration. In the case of Na, one hypothesis is that Na lowers the barrier for CO dissociation, resulting in carbide formation.[8a,24a] However, this explanation alone cannot explain the formation of Co_2C due to the very high activation energy for C diffusion in Co.[26] This high activation barrier kinetically prevents the diffusion of C into Co and we will discuss this in more detail below. Furthermore, recent studies have noted that there is already a high coverage of C species on Co during syngas conversion[27], and our ex situ XPS data of the spent Co catalyst agrees with this. Next, we note that prior work has found Co_2C catalysts to be stable in syngas for extended periods[22,24b] and we calculated that Co_2C is stable relative to *fcc*-Co by 1.2 eV on a per unit cell basis at the conditions used in this study. Since Co_2C is thermodynamically favorable, we conclude that there must be a kinetic limitation to its formation.

To investigate the kinetic barriers to Co_2C formation, we utilized DFT to study the diffusion of C into the Co (211) surface. The Co (211) surface was chosen because we found that Zn strongly interacts with this surface (Table S10). Calculations were performed to compare the energetics of C diffusion and transport on the Co (211) surface with and without Zn decoration, and the results are presented in Figure 6. Figure 6c

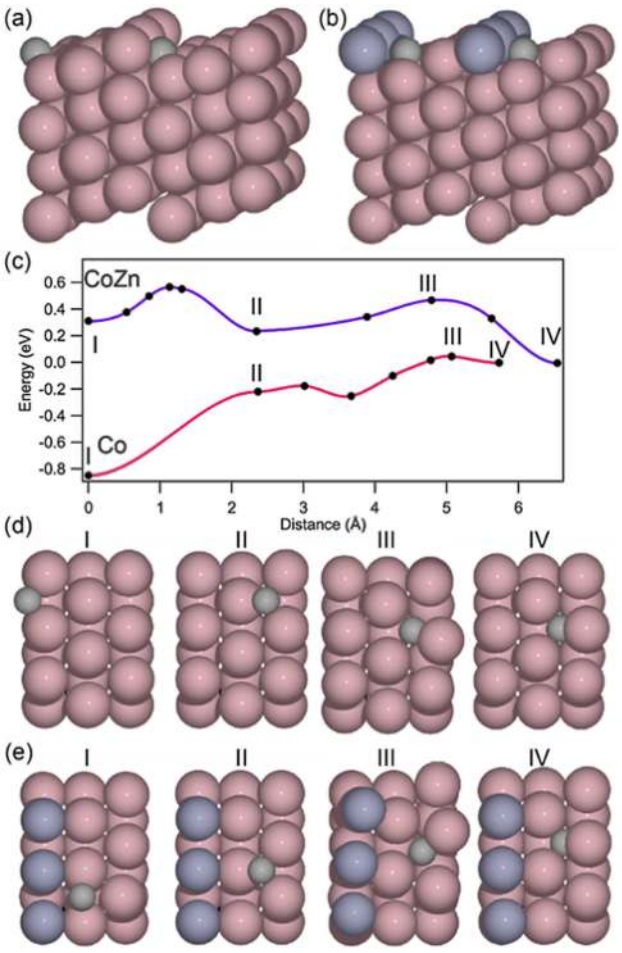

Figure 6. Carbon binding sites for (a) Co (211) and (b) Zn-decorated Co (211). Calculated potential energy profiles (c) for C diffusion using NEB for Co (211) in pink and Zn on Co (211) in purple. Energies are referenced to the final state with C subsurface. Marked points correspond to frames calculated using the NEB and the curve is a spline interpolation. Subfigures (d) and (e) show frames illustrating the diffusion pathways determined using the NEB calculation. Co atoms are shown in pink, Zn in purple, and C in grey with the Roman numerals on each frame corresponding to the frames point on the NEB curves.

shows the calculated energy profiles for C diffusion and transport on these surfaces. We find that the most stable site for C is the four-fold (B5) site below the Co step (Figure 6a). When Zn is added to the Co (211) surface (Figure 6b), Zn is most stable at the same binding site as C, binding below the Co (211) step. Thus, Zn blocks C from binding at this site and results in a much weaker binding energy of C to the Co (211) surface (Figure 6c). On the Zn-decorated Co (211) surface, the activation barriers for C diffusion are much smaller than for Co (Figure 6c). When examining the reverse reaction, we find that it is easier for subsurface carbon to move to the clean Co (211) surface. For the Zn-decorated Co (211) surface, diffusion of C from the subsurface to the surface is associated with a higher barrier. This may inhibit Co_2C decomposition as there is a higher barrier for the removal of C in the presence of Zn (see below). These DFT results support the more facile formation of Co_2C from the Zn/Co catalyst than from Co alone.

Prior work has associated the Co_2C phase both with promoting higher alcohol synthesis[4c,f,6a, 25] and with methane selectivity during CO hydrogenation.[17c] We found experimentally that Co_2C is selective toward methane without Zn and more selective towards alcohols with Zn present (Figure 3 and Table 2). Thus, we posit that changes in Co_2C structure result in a transition from selectivity towards hydrocarbons to selectivity towards alcohols[4f,24b,28].

Selectivity during CO hydrogenation can be related to the OH and CO binding energies that are used as descriptors for microkinetic modeling screening studies under the assumption of scaling relations. This analysis showed that Co (111) is very close to the peak of the volcano for higher alcohol synthesis.[3a] In this work, we calculated OH binding energies of −0.36 and −0.33 eV for the Co (111) and Co_2C (111) surfaces, respectively. We also calculated CO binding energies of −1.51 and −1.86 eV for the Co (111) and Co_2C (111) surfaces, respectively. This change in CO binding energy for the Co_2C (111) surface would shift away from the position of Co (111) on the CO hydrogenation volcano[3a] and would suggest that Co_2C (111) is more hydrocarbon selective in agreement with the prior results discussed above.

Given the sensitivity of the product distribution to the exposed crystal facets on Co_2C, we consider the role that Zn might play in changing which facets are available for reaction. Specifically, we attribute the higher selectivity and lower activity of Zn/Co catalysts compared to control Co_2C catalysts to the preferential passivation of unselective Co_2C crystal facets by Zn. When the unselective crystal facets are blocked, the catalyst's activity will drop as there is a loss of active sites and the selectivity will improve. Similar behavior has been observed in the case of Rh catalysts, where there was likewise an inverse relationship between selectivity and activity for higher alcohol synthesis.[5,29] Those studies demonstrated that the changes in activity and selectivity could be explained by the ratio of Rh (111) and Rh (211) areas exposed.[5,29] Similarly, we propose here that the Zn promoter influences the ratio of different crystal faces of Co_2C that are exposed and in this way impacts the activity and selectivity. In particular, increasing the relative amount of exposed Co_2C (111) facets could improve the selectivity.[4f]

Based on this discussion, we attribute the enhanced higher-alcohol selectivity of our prepared ALD-Zn/Co catalysts to a dual role of the Zn promoter. First, the Zn facilitates the formation of a Co_2C phase. Our in situ characterization supports this restructuring and the formation of metallic Zn, and our calculations provide a mechanism of how Zn enables the conversion of Co to Co_2C. Second, in addition to enabling Co_2C formation, the Zn blocks non-selective sites on the Co_2C surface, improving the selectivity towards higher alcohols.

Conclusions

In this study, we modified Co catalysts using ZnO deposited by ALD. The ZnO modification enhanced selectivity for alcohols and suppressed hydrocarbon formation. XRD and XAFS showed

that the ZnO-modified catalysts converted to Co_2C during operation. DFT indicated that the presence of Zn modified the electronic interaction of surface C with Co, resulting in Co_2C formation. The catalysts modified using ZnO exceeded the selectivity of control Co_2C catalysts made without ZnO. This leads to the conclusion that ZnO acts as a dual role promoter, both allowing for Co_2C formation and controlling which Co_2C crystal facets are exposed, resulting in the observed selectivity trends. This work provides new insights into Co_2C formation and the effects of promoters on Co that will aid in designing new catalysts for alcohol synthesis from syngas.

Experimental Section

Synthesis and Characterization

Cobalt catalysts were synthesized by incipient wetness impregnation. Silica gel (Davisil grade 643, Aldrich) was impregnated with Co $(NO_3)_2 \cdot 6H_2O$ in deionized water. Samples were dried at room temperature and then calcined in air at 350 °C for 4 hours.

Zinc oxide ALD was performed using a Gemstar reactor (Arradiance). The deposition procedure was similar to those of prior studies.[3b,8b] Samples were cleaned using UV irradiation and ozone prior to deposition. Custom stainless steel powder holders consisting of a stainless steel petri dish and a fine mesh cover to contain the powders were used during the ALD process based on procedure by Libera *et al.*[12c] The deposition was performed at 150 °C in exposure mode, in which the reactant gasses are held in the reactor for a fixed time after pulsing. In each cycle, diethyl zinc (Aldrich) was pulsed for 0.1 s and exposed for 30 s, the reactor was purged for 180 s with nitrogen gas, water vapor was pulsed for 0.1 s and exposed for 30 s, and the reactor was purged for 180 s with nitrogen gas.

A Micromeritics 3 Flex instrument was used for nitrogen physisorption measurements. Surface areas were calculated applying Brunauer-Emmett-Teller (BET) method. The Barett-Joyner-Halenda (BJH) method was used to calculate pore sizes.

Inductively coupled plasma optical emission spectrometry (ICP-OES) was performed using a Thermo Fisher ICAP 6300 Duo View ICP-OES spectrometer to characterize the ZnO mass deposited using the ZnO ALD process. Samples were digested in boiling nitric acid to prepare for ICP-OES. High-purity standards were obtained from Aldrich and diluted.

Elemental mapping was performed in scanning TEM mode with energy-dispersive X-ray spectroscopy (EDS) performed using an Oxford X-Max solid-state silicon drift detector. The Co $K_{\alpha 1}$ and Zn $K_{\alpha 1}$ lines were used for the EDS analysis. Samples were drop-cast on copper-supported ultrathin carbon TEM grids (Ted Pella).

CO chemisorption experiments were performed by loading 90 mg of catalyst into a quartz U-tube. Temperature programmed reduction (TPR) was performed on the catalysts in a 10% H_2/Ar mixture, using a ramp rate of 10 °C/min up to 550 °C. After cooling the catalyst to 30 °C, CO chemisorption was performed by pulsing a fixed volume of 10% CO/He across the catalyst and recording the CO consumption by a thermal conductivity detector (TCD). The CO pulses were repeated until full saturation was reached, as measured by a constant CO signal. The CO uptake by the catalyst was calculated from the areas of the TCD pulse signals.

XPS data were collected using a PHI Versaprobe 3 with Al K_α radiation (1486.6 eV). Dual ion and electron neutralization was used to minimize the effects of sample charging. The X-ray beam diameter was 200 μm with 42 W power. Samples were prepared by pressing catalyst powder into carbon tape mounted on a Si wafer.

Catalytic Testing

Catalyst performance was evaluated using an Altamira Benchcat 4000 HP packed bed reactor system. Carbon monoxide (Airgas, 5.0 purity) was purified by passing through a 300 °C alumina bed to decompose metal carbonyl impurities. Catalysts were packed in an inert-coated (Silcolloy or glass) 0.25 inch outer diameter stainless steel tube. In each test, a catalyst was packed between two plugs of quartz wool above a bed of glass beads. The Co/SiO_2 catalysts were diluted using silica gel (Aldrich) to distribute the small mass of catalyst used in the testing. Samples were reduced in H_2 (Airgas, 5.0 purity) by ramping at 10 °C/min to 450 °C and holding for 1 hour. Samples were cooled while building pressure to 20 bar in H_2. Upon reaching 250 °C, the gas stream was switched to a flow of 2:1 H_2:CO while maintaining a pressure of 20 bar. The effluent was analyzed using an online Agilent 7890B gas chromatograph-mass spectrometer. Products were quantified using a flame ionization detector. Conversions were calculated based on the detected products. Carbon-weighted selectivities are reported in which the product yield is multiplied by the carbon count of the product.

The concentration of CO converted to products was found by adding the concentration of each product weighted by the carbon count of the product. The sum of the carbon-weighted concentrations of higher oxygenates was divided by the total concentration of CO converted to products to yield the higher oxygenate selectivity. The fraction of CO converted was calculated by dividing the concentration of CO converted to products by the concentration of CO in the gas feed, determined by the H_2 and CO flow rates. Activities were determined by converting this fraction into the molar rate of CO conversion, based on the CO flow rate, and dividing by the mass of catalyst loaded into the reactor.

In situ X-ray Diffraction (XRD)

In situ XRD was performed at Stanford Synchrotron Radiation Lightsource (SSRL) at beamline 2-1. Incident photon energy was set to 15.5 keV (0.801 Å) using a Si (111) double-crystal monochromator and a Pilatus 100k detector was used to collect diffraction patterns. An XRD scan was acquired every 2 minutes during the reduction and every 10 minutes during measurements at reaction conditions. Samples were contained within a custom reactor as previously described.[30] Samples were packed in glass capillaries between two plugs of quartz wool. Gas flows were controlled using mass flow controllers (MFC, Brooks) and the pressure was controlled using a back-pressure regulator (Swagelok). Temperature was controlled using a Cryocon PID controller and a K-type thermocouple inserted inside the capillary. CO was purified using a Nanochem Metal-X (Matheson) purifier. Samples were reduced in flowing H_2 at 10 °C/minute to 450 °C. After reduction, measurements under reaction conditions were performed at 250 °C in flowing 2:1 H_2:CO at 20 bar. Carburization of Co/SiO_2 was performed in situ at 250 °C in 20 bar CO. Decarburization was performed in H_2 at atmospheric pressure. For safety reasons, all experiments were performed in a ventilated experimental hutch and using a Kapton safety shield surrounding the glass capillary.

In situ X-ray Absorption Fine Structure (XAFS)

XAFS measurements were performed at SSRL at beamline 2–2. Extended X-ray absorption fine structure (EXAFS), and X-ray

absorption near edge structure (XANES) data was recorded at the Co K-edge (7709 eV) and Zn K-edge (9659 eV) by step-scanning the Si (220) (crystal orientation $\varphi = 0°$) double-crystal monochromator. The XAFS spectra were collected in transmission mode while simultaneously collecting the spectra of Co or Zn foil for energy-calibration. Commercial Co_3O_4, and ZnO powders (Aldrich) were used as standards. EXAFS spectra were collected every 20 minutes while the catalyst was at a steady state and multiple spectra were collected to improve signal-to-noise. XANES spectra were collected every 7 minutes and were used to monitor the transient states of the catalysts.

Heating and gas exposure of the catalyst was conducted using a glassy carbon tube reactor (Sigradur, 0.25 inch outer diameter, 0.125 inch inner diameter) and held into a stainless steel heated block as described previously.[31] Catalysts were loaded into the reactor between plugs of quartz wool. Heating was provided by two 100 W cartridge heaters inserted into the stainless-steel block and regulated by a Eurotherm controller with a K-type thermocouple mounted inside the glassy carbon tube near the catalyst bed. CO purified using a Nanochem Metal-X (Matheson) purifier, H_2 and He were dosed by MFCs (Brooks). The system pressure was controlled using a back-pressure regulator (Swagelok).

Initially, EXAFS spectra were recorded of the as-loaded sample under flowing helium at room temperature. A temperature-programmed reduction was performed by heating the catalyst in pure H_2 to 450 °C at 5 °C/min followed by cooling down in the H_2 flow to 250 °C. XANES spectra were collected during the temperature ramp and EXAFS spectra were collected after the in situ reduction to characterize the reduced sample. Subsequently a mixture of 2:1 H_2:CO was dosed and the reactor was pressurized to 20 bar at 250 °C. Once at pressure, XANES spectra were recorded until there were no detectable changes in spectra, indicating steady state had been achieved. EXAFS spectra were recorded characterizing the steady state structure of the catalyst under working conditions. This step was repeated with a reaction temperature of 300 °C. In the case of the Co/SiO_2, the catalyst was exposed to 20 bar CO at 250 °C in an analogous manner, concluding the experiment with an EXAFS spectrum at 250 °C to form Co_2C/SiO_2 in situ.

The raw XAFS data was processed using the Athena software in the Demeter package.[32] All spectra were energy calibrated, aligned, merged, and normalized. XANES spectra were analyzed using linear combination fitting. XANES spectra of Co metal foil, bulk Co_3O_4 and CoO, and Co_2C nanoparticles supported on SiO_2 were used as standards for the fitting.

EXAFS functions were extracted in the Athena software with modelling of the EXAFS completed using the Artemis software the Demeter package.[32] Absorber-backscatter scattering paths used in the models were simulated from crystallographic data of bulk compounds using FEFF6.[33] EXAFS models were optimized using k^1, k^2, and k^3 weightings with all models obeying the Nyquist criterion[33] in k-space and Fourier-transformation was conducted on the k^3-weighted EXAFS function ($k = 3.0–12.5$ Å^{-1}) to amplify the oscillations at high k-values. Phase shifts and amplitudes for relevant back-scattering paths were calculated and EXAFS refinement was carried out on an R-range of 1.0–3.0 Å. For Co K-edge spectra, crystallographic data of Co_3O_4 was used to model as-prepared catalysts, *hcp*-Co for nearest-neighbor coordination shells of metallic Co, Co_2C for bulk cobalt carbide and $Co_2(CO)_8$ for Co–O and Co–C–O paths characteristic for linearly bonded carbonyl groups. For Zn K-edge spectra, crystallographic data of ZnO was used to model the nearest-neighbor Zn–O coordination shell in Zn-containing catalysts. Packets of characteristic scattering paths were robustly fitted to the experimental data using proportionally scaled coordination numbers to quantify the fraction of the given chemical species.

The carbide/metal ratio in 4 ALD Zn/Co under reaction conditions was determined from EXAFS by dividing the scaling factor of the carbide model fit by the sum of scaling factors of carbide and metal. This was justified by the similarity of the two structures[18] and the assumption that carbide was formed only by carbon insertion into the metal lattice and corresponding slight lattice expansion, but no sintering or re-dispersion of the catalyst particles.

The fitting used shared edge energy corrections (ΔE_0), bond distance corrections (shift in *d*) and mean square thermal displacements (σ^2). Amplitude reduction factors (S_0^2) were determined by fitting EXAFS spectra of reference compounds with tabulated coordination numbers. A value of $S_0^2 = 0.73 \pm 0.04$ from the fit of Co foil was used for all fits and was consistent with $S_0^2 = 0.72 \pm 0.04$ from the fit of Co_3O_4 reference. For Zn K-edge spectra, $S_0^2 = 0.96$ determined from the fit of ZnO was used.

Density Functional Theory Calculations

Periodic DFT calculations were carried out using the Quantum Espresso code[34] in connection with the Atomic Simulation Environment.[35] The BEEF-vdW exchange correlation functional was used as it was specifically developed to describe both chemisorption and physisorption properties of adsorbates.[36] A plane-wave cut-off of 500 eV and a density cut-off of 5000 eV were used for all calculations. The ionic cores were described using Vanderbilt ultrasoft pseudopotentials.[37] Spin-polarized calculations were performed for all Co containing systems. The Co metal slab models were based on 3×3×4 supercells, which were separated by 20 Å of vacuum space in the direction perpendicular to the surface plane. Co_2C slabs were based on 2×2×4 supercells and separated by 16 Å vacuum space. The top two atomic layers of the slab models were allowed to relax whereas the bottom two were fixed at their bulk positions. The Brillouin zones were sampled using a 4×4×1 Monkhorst-Pack k-point mesh.[38] The convergence criterion for the energy optimization was a maximum force of 0.05 eV/Å per atom. Transition states for carbon subsurface diffusion were calculated using the nudged elastic band (NEB) method.[39]

Acknowledgements

We acknowledge financial support from the U.S. Department of Energy, Office of Basic Energy Sciences to the SUNCAT Center for Interface Science and Catalysis. This material is based upon work supported by the National Science Foundation Graduate Research Fellowship under Grant No. DGE-114747. Co-ACCESS, is supported by the U.S. Department of Energy, Office of Science, Office of Basic Energy Sciences, Chemical Sciences, Geosciences and Biosciences under Contract DE-AC02-76SF00515. Use of the Stanford Synchrotron Radiation Lightsource, SLAC National Accelerator Laboratory, is supported by the U.S. Department of Energy, Office of Science, Office of Basic Energy Sciences under Contract No. DE-AC02-76SF00515. A part of this work was supported by a postdoc fellowship of the German Academic Exchange Service (DAAD) to Julia Schumann. The authors gratefully acknowledge the use of the Stanford Nano Shared Facilities (SNSF) of Stanford University for sample characterization. The authors would like to thank Andrew Riscoe for performing the BET measurements.

Conflict of Interest

The authors declare no conflict of interest.

Keywords: Higher alcohol synthesis · in situ characterization · EXAFS modelling · cobalt carbide · density functional theory

[1] F. Fischer, H. Tropsch, *Brennstoff-Chem.* **1923**, *4*, 276–285.

[2] H. T. Luk, C. Mondelli, D. C. Ferré, J. A. Stewart, J. Pérez-Ramírez, *Chem. Soc. Rev.* **2017**, *46*, 1358–1426.

[3] a) J. Schumann, A. J. Medford, J. S. Yoo, Z.-J. Zhao, P. Bothra, A. Cao, F. Studt, F. Abild-Pedersen, J. K. Nørskov, *ACS Catal.* **2018**, *8*, 3447–3453; b) J. A. Singh, N. Yang, X. Liu, C. Tsai, K. H. Stone, B. Johnson, A. L. Koh, S. F. Bent, *J. Phys. Chem. C* **2018**, *122*, 2184–2194; c) J. J. Spivey, A. Egbebi, *Chem. Soc. Rev.* **2007**, *36*, 1514–1528.

[4] a) Z. An, X. Ning, J. He, *J. Catal.* **2017**, *356*, 157–164; b) M. Ao, G. H. Pham, J. Sunarso, M. O. Tade, S. Liu, *ACS Catal.* **2018**, 7025–7050; c) Y.-P. Pei, J.-X. Liu, Y.-H. Zhao, Y.-J. Ding, T. Liu, W.-D. Dong, H.-J. Zhu, H.-Y. Su, L. Yan, J.-L. Li, W.-X. Li, *ACS Catal.* **2015**, *5*, 3620–3624; d) V. Subramani, S. K. Gangwal, **2008**, 814–839; e) Y. Xiang, V. Chitry, P. Liddicoat, P. Felfer, J. Cairney, S. Ringer, N. Kruse, *J. Am. Chem. Soc.* **2013**, *135*, 7114–7117; f) R. Zhang, G. Wen, H. Adidharma, A. G. Russell, B. Wang, M. Radosz, M. Fan, *ACS Catal.* **2017**, 8285–8295.

[5] N. Yang, A. J. Medford, X. Liu, F. Studt, T. Bligaard, S. F. Bent, J. K. Norskov, *J. Am. Chem. Soc.* **2016**, *138*, 3705–3714.

[6] a) G. G. Volkova, T. M. Yurieva, L. M. Plyasova, M. I. Naumova, V. I. Zaikovskii, *J. Mol. Catal. A* **2000**, *158*, 389–393; b) X.-C. Xu, J. Su, P. Tian, D. Fu, W. Dai, W. Mao, W.-K. Yuan, J. Xu, Y.-F. Han, *J. Phys. Chem. C* **2015**, *119*, 216–227.

[7] a) V. P. Santos, B. Van Der Linden, A. Chojecki, G. Budroni, S. Corthals, H. Shibata, G. R. Meima, F. Kapteijn, M. Makkee, J. Gascon, *ACS Catal.* **2013**, *3*, 1634–1637; b) K. Simeonov, J. H. Kim, D. Ferrari, D. Huelsman, G. Budroni, S. Corthals, Y. J. Pagán-Torres, *Catal. Sci. Technol.* **2014**, *4*, 922–922.

[8] a) Z. Li, L. Zhong, F. Yu, Y. An, Y. Dai, Y. Yang, T.-J. Lin, S. Li, H. Wang, P. Gao, Y. Sun, M. He, *ACS Catal.* **2017**, acscatal.6b03478-acscatal.03476b03478; b) N. Yang, J. S. Yoo, J. Schumann, P. Bothra, J. A. Singh, E. Valle, F. Abild-Pedersen, J. K. Nørskov, S. F. Bent, *ACS Catal.* **2017**, *7*, 5746–5757.

[9] a) N. N. Madikizela-Mnqanqeni, N. J. Coville, *Appl. Catal. A* **2007**, *317*, 195–203; b) N. N. Madikizela, N. J. Coville, *J. Mol. Catal. A* **2002**, *181*, 129–136; c) Y. Xing, Z. Liu, Y. Xue, D. Wu, S. Fang, *Catal. Lett.* **2016**, *146*, 1–10.

[10] J. Llorca, A. Barbier, G. A. Martin, J. Sales, P. Ramírez De La Piscina, N. Homs, *Catal. Lett.* **1996**, *42*, 87–91.

[11] a) J. Lu, J. W. Elam, P. C. Stair, *Surf. Sci. Rep.* **2016**, *71*, 410–472; b) B. J. O'Neill, D. H. K. Jackson, J. Lee, C. Canlas, P. C. Stair, C. L. Marshall, J. W. Elam, T. F. Kuech, J. A. Dumesic, G. W. Huber, *ACS Catal.* **2015**, *5*, 1804–1825; c) J. A. Singh, N. Yang, S. F. Bent, *Annu. Rev. Chem. Biomol. Eng.* **2017**, *8*, 41–62.

[12] a) J. Camacho-Bunquin, P. Aich, M. Ferrandon, A. "Bean" Getsoian, U. Das, F. Dogan, L. A. Curtiss, J. T. Miller, C. L. Marshall, A. S. Hock, P. C. Stair, *J. Catal.* **2017**, *345*, 170–182; Getsoian, U. Das, F. Dogan, L. A. Curtiss, J. T. Miller, C. L. Marshall, A. S. Hock, P. C. Stair, *J. Catal.* **2017**, *345*, 170–182; b) E. Guziewicz, M. Godlewski, L. Wachnicki, T. A. Krajewski, G. Luka, S. Gieraltowska, R. Jakiela, A. Stonert, W. Lisowski, M. Krawczyk, J. W. Sobczak, A. Jablonski, *Semicond. Sci. Technol.* **2012**, *27*, 074011–074011; c) J. A. Libera, J. W. Elam, M. J. Pellin, *Thin Solid Films* **2008**, *516*, 6158–6166; d) M. N. Mullings, C. Hägglund, J. T. Tanskanen, Y. Yee, S. Geyer, S. F. Bent, *Thin Solid Films* **2014**, *556*, 186–194.

[13] M. H. Chu, L. Tian, A. Chaker, V. Cantelli, T. Ouled, R. Boichot, A. Crisci, S. Lay, M. I. Richard, O. Thomas, J. L. Deschanvres, H. Renevier, D. D. Fong, G. Ciatto, *Crystal Growth and Design* **2016**, *16*, 5339–5348.

[14] a) M. C. Biesinger, B. P. Payne, A. P. Grosvenor, L. W. M. Lau, A. R. Gerson, R. S. C. Smart, *Appl. Surf. Sci.* **2011**, *257*, 2717–2730; b) A. A. Khassin, T. M. Yurieva, V. V. Kaichev, V. I. Bukhtiyarov, A. A. Budneva, E. A. Paukshtis, V. N. Parmon, *J. Mol. Catal. A* **2001**, *175*, 189–204.

[15] M. N. Islam, T. B. Ghosh, K. L. Chopra, H. N. Acharya, *Thin Solid Films* **1996**, *280*, 20–25.

[16] a) K. H. Cats, B. M. Weckhuysen, *ChemCatChem* **2016**; b) D. I. Enache, B. Rebours, M. Roy-Auberger, R. Revel, *J. Catal.* **2002**, *205*, 346–353; c) V. M. Lebarbier, D. Mei, D. H. Kim, A. Andersen, J. L. Male, J. E. Holladay, R. Rousseau, Y. Wang, *J. Phys. Chem. C* **2011**; d) M. Rønning, N. E. Tsakoumis, A. Voronov, R. E. Johnsen, P. Norby, W. van Beek, Ø. Borg, E. Rytter, A. Holmen, *Catal. Today* **2010**, *155*, 289–295.

[17] a) M. K. Gnanamani, G. Jacobs, U. M. Graham, M. C. Ribeiro, F. B. Noronha, W. D. Shafer, B. H. Davis, *Catal. Today* **2016**, *261*, 40–47; b) G. Kwak, M. H. Woo, S. C. Kang, H. G. Park, Y. J. Lee, K. W. Jun, K. S. Ha, *J. Catal.* **2013**, *307*, 27–36; c) J. C. Mohandas, M. K. Gnanamani, G. Jacobs, W. Ma, Y. Ji, S. Khalid, B. H. Davis, *ACS Catal.* **2011**, *1*, 1581–1588.

[18] O. Ducreux, B. Rebours, J. Lynch, M. Roy-Auberger, D. Bazin, *Oil Gas Sci. Technol.* **2009**, *64*, 49–62.

[19] a) H. Karaca, J. Hong, P. Fongarland, P. Roussel, A. Griboval-Constant, M. Lacroix, K. Hortmann, O. V. Safonova, A. Y. Khodakov, *Chemical communications (Cambridge, England)* **2010**, *46*, 788–790; b) N. E. Tsakoumis, A. Voronov, M. Ronning, W. V. Beek, O. Borg, E. Rytter, A. Holmen, *J. Catal.* **2012**, *291*, 138–148.

[20] a) B. Ernst, A. Bensaddik, L. Hilaire, P. Chaumette, A. Kiennemann, *Catal. Today* **1998**, *39*, 329–341; b) A. Rochet, V. Moizan, C. Pichon, F. Diehl, A. Berliet, V. Briois, *Catal. Today* **2011**, *171*, 186–191.

[21] a) J. Xiong, Y. Ding, T. Wang, L. Yan, W. Chen, H. Zhu, Y. Lu, *Catal. Lett.* **2005**, *102*, 265–269; b) E. Varga, Z. Ferencz, A. Oszkó, A. Erdőhelyi, J. Kiss, *J. Mol. Catal. A* **2015**, *397*, 127–133.

[22] M. Claeys, M. E. Dry, E. Van Steen, E. Du Plessis, P. J. Van Berge, A. M. Saib, D. J. Moodley, *J. Catal.* **2014**, *318*, 193–202.

[23] S. Kuld, M. Thorhauge, H. Falsig, C. F. Elkjaer, S. Helveg, I. Chorkendorff, J. Sehested, *Science* **2016**, *352*, 969–974.

[24] a) C. Mirodatos, E. Brum Pereira, A. Gomez Cobo, J. A. Dalmon, G. A. Martin, *Top. Catal.* **1995**, *2*, 183–192; b) L. Zhong, F. Yu, Y. An, Y. Zhao, Y. Sun, Z. Li, T. Lin, Y. Lin, X. Qi, Y. Dai, L. Gu, J. Hu, S. Jin, Q. Shen, H. Wang, *Nature* **2016**, *538*, 84–87.

[25] H. Du, H. Zhu, X. Chen, W. Dong, W. Lu, W. Luo, M. Jiang, T. Liu, Y. Ding, *Fuel* **2016**, *182*, 42–49.

[26] D. Moodley, J. van de Loosdrecht, H. Niemantsverdriet, A. Saib, **2009**.

[27] a) M. Corral Valero, P. Raybaud, *J. Phys. Chem. C* **2014**, *118*, 22479–22490; b) V. Navarro, M. A. van Spronsen, J. W. M. Frenken, *Nat. Chem.* **2016**, *8*, 929–934.

[28] J. Cheng, P. Hu, P. Ellis, S. French, G. Kelly, C. M. Lok, *J. Phys. Chem. C* **2010**, *114*, 1085–1093.

[29] N. Yang, X. Liu, A. S. Asundi, J. K. Nørskov, S. F. Bent, *Catal. Lett.* **2017**, *0*, 1–18.

[30] A. S. Hoffman, J. A. Singh, S. F. Bent, S. R. Bare, *J. Synchrotron Radiat.* **2018**, *25*.

[31] A. M. Karim, C. Howard, B. Roberts, L. Kovarik, L. Zhang, D. L. King, Y. Wang, *ACS Catal.* **2012**, *2*, 2387–2394.

[32] B. Ravel, M. Newville, *J. Synchrotron Radiat.* **2005**, *12*, 537–541.

[33] J. J. Rehr, J. J. Kas, F. D. Vila, M. P. Prange, K. Jorissen, *Phys. Chem. Chem. Phys.* **2010**, *12*, 5503–5503.

[34] P. Giannozzi, S. Baroni, N. Bonini, M. Calandra, R. Car, C. Cavazzoni, D. Ceresoli, G. L. Chiarotti, M. Cococcioni, I. Dabo, A. Dal Corso, S. de Gironcoli, S. Fabris, G. Fratesi, R. Gebauer, U. Gerstmann, C. Gougoussis, A. Kokalj, M. Lazzeri, L. Martin-Samos, N. Marzari, F. Mauri, R. Mazzarello, S. Paolini, A. Pasquarello, L. Paulatto, C. Sbraccia, S. Scandolo, G. Sclauzero, A. P. Seitsonen, A. Smogunov, P. Umari, R. M. Wentzcovitch, *J. Phys. Condens. Matter* **2009**, *21*, 395502–395502.

[35] S. R. Bahn, K. W. Jacobsen, *Comput. Sci. Eng.* **2002**, *4*, 56–66.

[36] J. Wellendorff, K. T. Lundgaard, A. Møgelhøj, V. Petzold, D. D. Landis, J. K. Nørskov, T. Bligaard, K. W. Jacobsen, *Physical Review B - Condensed Matter and Materials Physics* **2012**, *85*, 32–34.

[37] K. Laasonen, R. Car, C. Lee, D. Vanderbilt, *Phys. Rev. B* **1991**, *43*, 6796–6799.

[38] H. J. Monkhorst, J. D. Pack, *Phys. Rev. B* **1976**, *13*, 5188–5192.

[39] H. Jónsson, G. Mills, K. W. Jacobsen, *Classical and Quantum Dynamics in Condensed Phase Simulations* **1998**, 385–404.

Manuscript received: October 23, 2018
Revised manuscript received: November 30, 2018
Accepted manuscript online: December 4, 2018
Version of record online: December 27, 2018